

***Final Draft***  
**of the original manuscript:**

Yu, Z.; Huang, Y.; Mendis, C.L.; Hort, N.; Jian, M.:

**Microstructural evolution and mechanical properties of  
Mg–11Gd–4.5Y–1Nd–1.5Zn–0.5Zr alloy prepared via pre-ageing  
and hot extrusion**

In: Materials Science and Engineering A (2014) Elsevier

DOI: 10.1016/j.msea.2014.11.061

# Microstructural evolution and mechanical properties of Mg-11Gd-4.5Y-1Nd-1.5Zn-0.5Zr alloy prepared via pre-ageing and hot extrusion

Zijian Yu<sup>a,b,c</sup>, Yuanding Huang<sup>b</sup>, Chamini Lakshi Mendis<sup>b</sup>, Norbert Hort<sup>b</sup>, Jian Meng<sup>a\*</sup>

*a. State Key Laboratory of Rare Earth Resources Utilization, Changchun Institute of Applied Chemistry, Chinese Academy of Sciences, Changchun 130022, P. R. China*

*b. MagIC-Magnesium Innovation Centre, Helmholtz-Zentrum Geesthacht, Max-Planck-Str. 1, D-21502 Geesthacht, Germany*

*c. University of Chinese Academy of Sciences, Beijing 100049, P. R. China*

## Abstract

The Mg-11Gd-4.5Y-1Nd-1.5Zn-0.5Zr (wt.%) alloy was pre-aged prior to hot extrusion. Pre-ageing treatment introduced uniform distribution of plate-like Mg<sub>5</sub>RE precipitates, which transformed into nano-scale globular Mg<sub>5</sub>RE particles by split and spheroidization during hot extrusion. These globular Mg<sub>5</sub>RE particles contributed to continuous dynamic recrystallization by promoting the evolution of low misorientation sub-grain boundaries to high misorientation grain boundaries and caused grain refinement through grain boundary pinning. The improved mechanical properties were ascribed to the grain refinement, globular Mg<sub>5</sub>RE and LPSO precipitates. The ratio of compressive to tensile yield strength is 1.2. The yield strength asymmetry was attributed to the deformation asymmetry of LPSO phase and non-isotropic deformation behaviours of Mg matrix in tension and compression.

*Keywords:* Pre-ageing; Precipitates; Deformation; Recrystallization; Mechanical properties

\*Corresponding author. Tel: +86-431 85262030; Fax: +86-431 85698041

E-mail address: jmeng@ciac.jl.cn (Jian Meng)

# 1. Introduction

There is considerable interest in the development of rare earth (RE) containing Mg alloys with high strength, high toughness, heat resistance and good ductility. Desired properties profile may be obtained through optimization of microstructure, including grain refinement, precipitation and texture control, through various thermo-mechanical treatments such as hot rolling and extrusion [1-8].

The age-hardening response of Mg-RE alloys has been investigated with or without other alloying elements such as Zn and Ag [9-14]. The additions of Zn and Ag contribute to the increase in maximum hardness by promoting the formation of basal plate-like precipitates that are few atomic layers thick [13, 14]. The metastable  $\beta'$  phase forms on the prismatic plane of  $\{\bar{1}100\}_\alpha$  of  $\alpha$ -Mg matrix and plays an important role in strengthening by hindering the glide of basal dislocations [15]. Thus, there is potential to develop ultra-high strength Mg-RE alloys through precipitation [1-4]. Several disadvantages, such as slow age hardening response and coarsening of metastable phases with further exposure to elevated temperature, limit the wide use of these alloys [11-13].

Recent investigations show that equilibrium phases, such as  $Mg_5RE$  phase in RE containing Mg alloys, influence the dynamic recrystallization (DRX) and texture evolution during deformation and result in grain refinement and strengthening of the deformed Mg alloys [2, 3, 16, 17]. In Mg-RE alloys, the equilibrium  $Mg_5RE$  phase particles with various morphologies and distributions are observed due to different formation mechanisms. The first is the plate-like  $Mg_5RE$  particles that form on  $\{\bar{1}100\}_\alpha$  planes of  $\alpha$ -Mg matrix during long term isothermal ageing [11]. Second is globular  $Mg_5RE$  particles that form at the grain

boundaries due to dynamic precipitation during hot deformation [1, 2]. In comparison with the coarse plate-like Mg<sub>5</sub>RE particles, the dense and uniform globular Mg<sub>5</sub>RE particles improve the mechanical properties of the deformed Mg-RE alloys [2]. However, controlling the morphology and quantity of equilibrium Mg<sub>5</sub>RE phase in deformed Mg-RE alloys, and corresponding mechanisms remain unclear. The recrystallization behaviour of Mg-RE alloys containing Mg<sub>5</sub>RE particles is also difficult to be predicted, as it depends on whether the particles precipitate before plastic deformation or during recrystallization; and the nature and dispersion of the particles [16, 18-20].

The Zn addition to Mg-RE alloys forms long period stacking ordered (LPSO) phase, which significantly **strengthens** the Mg alloys via short-fibre strengthening [21-23]. The deformation behaviour of LPSO phase depends on the loading direction due to the strong plastic anisotropy caused by the layered structure [21, 22, 24]. Thus, Mg alloys containing LPSO phase are sensitive to microstructure and loading direction [21]. The deformation behaviour and strengthening mechanisms of LPSO phase under compression **have** been investigated. Kink bands **that form** in the LPSO phase during compressive deformation considerably improve the ductility of the alloys [23, 24]. However, the deformation mechanism of the LPSO phase in tension has not been clarified.

The purpose of this work is to investigate the microstructural evolution during pre-ageing and hot extrusion. The influences of second phase particles, including Mg<sub>5</sub>RE and LPSO phase, on the recrystallization **behaviour** and mechanical properties of a Mg-RE alloy will be explored.

## 2. Experimental procedures

Cylindrical billet of the Mg-11Gd-4.5Y-1.5Zn-1Nd-0.5Zr (wt.%) alloy was cast into a cylinder steel mould with a diameter of 92 mm at  $760 \pm 3$  °C under a mixture of SF<sub>6</sub>/CO<sub>2</sub> (1:99) protective atmosphere. The mould was preheated to  $200 \pm 3$  °C. The cylindrical billet was machined into a round bar with a diameter of 82 mm and a length of 120 mm, then homogenized at  $535 \pm 3$  °C for 24 hours and quenched in water (25 °C). Subsequently, homogenized sample was pre-aged at  $410 \pm 3$  °C for 1 h before hot extrusion at 410°C with a extrusion ratio of ~30:1 at a ram speed of  $1.0 \text{ mm}\cdot\text{s}^{-1}$ . In order to evaluate the phase evolution, the pre-aged samples (Pre-aged sample A) were further heat-treated at  $430 \pm 3$  °C and  $470 \pm 3$  °C for 2 h and referred to as Pre-aged sample B and C, respectively. The process histories of these samples were summarised in Table 1. Three tensile specimens (20 mm×4 mm×2 mm) and three compression specimens ( $\Phi$  11 mm×16.5 mm) were prepared with the extruded bar and tested parallel to the extrusion direction (ED) using an Instron 5569 tensile tester at an initial speed of  $1 \text{ mm}\cdot\text{min}^{-1}$  at room temperature. In order to investigate the deformation behaviour in tension and compression, the tensile and compressive tests were interrupted soon after yield in a separate set of samples, with a corresponding strain (including elastic deformation stage) of 3.3 % for the tensile specimen and 2.9 % for the compressive specimen. The samples for microstructural observations were taken from the central part of those deformed specimens. The fractured specimens were also investigated at a region close to the fracture surfaces.

The microstructures were observed with optical microscopy (OM) with a Leica DMI 5000 light optical microscope, scanning electron microscopy (SEM) using a Carl Zeiss Ultra

55 SEM equipped with an EDAX/TSL electron back scattered diffraction (EBSD) operating at 15kV, and transmission electron microscopy (TEM) using a Philips CM 200 TEM operating at 200 kV. The TEM specimens were prepared by mechanically grinding to a thickness of 120  $\mu\text{m}$  and then electro-polishing to perforation (2.5 % Perchloric acid and 97.5 % Ethanol, -47 °C, 40 V) using a twin jet **electro polisher**. To investigate the effect of pre-ageing on the **evolution** of microstructure and intermetallic phases during hot extrusion, two samples were cut for microstructural analysis from two different locations along the extruded bar: 10 mm (E10, partially deformed area) and 100 mm (E100, fully deformed area) from the front end of extruded bar, as shown in Table 1. X-ray diffraction (XRD) measurements were performed using the diffractometer on Siemens D5000 operating at 40 kV and 40 mA with Cu  $K_{\alpha}$  radiation and secondary monochromator with a step size of  $0.03^{\circ} \text{ s}^{-1}$  and a dwell time of 3 s. The volume fractions of the secondary phases were calculated from the average area of **these** particles using SEM/OM micrographs. The global texture was calculated **with** X-ray texture analysis on Panalytical X-ray diffractometer operating at 40kV and 40 mA.

### 3. Results

#### 3.1 Microstructural evolution

The microstructure after homogenization treatment contains LPSO phase at grain boundaries and inside grains (white arrows), Fig. 1a. The eutectic phase is located between **the** LPSO phase particles. As shown in Fig. 1b, a large number of plate-like precipitates form and distributed, in triangle arrays, in the  $\alpha$ -Mg matrix after pre-ageing at 410 °C for 1 hour (pre-aged sample A). In order to characterize the plate-like precipitates, the pre-aged sample A

was further aged at 430 °C (pre-aged sample B) and 470 °C (pre-aged sample C) for 2 hours. With the increased ageing temperature, the number of the plate-like precipitates gradually decreased. They were still observed in the matrix even after ageing at 470 °C for 2 h. Table 2 summarized the volume fraction of the plate-like particles observed for each pre-aged **condition**. The volume fraction of plate-like particles is  $10.7 \pm 1.3\%$  for the pre-aged sample A,  $10.2 \pm 0.7\%$  for the pre-aged sample B and  $4.9 \pm 1.5\%$  for the pre-aged sample C. The ageing treatments have a negligible effect on other precipitates, such as the LPSO phase and the eutectic phase, and the volume fraction of these phases did not **change significantly** in the pre-aged samples, **Table 2**.

Fig. 2a and b show the microstructures of sample E10 and E100. Due to partial deformation, irregular shaped nano-particles appeared in a form of “beaded strands” or “strings” along the ED in sample E10 as indicated by white arrows in Fig. 2a. The “string” consisted of nano-particles with similar dimensions **that** were aligned one after another. The nano-particles were separated from each other. **In addition to** the nano-particle strings, some plate-like particles **remain** in the matrix. Some of the plate-like particles show cracks as indicated by black arrows. The “strings” and the plate-like particles **were similar in size** and “strings” were aligned along the same directions as plates. Thus, the “string” nano-particles form by cracking of the plate-like particles due to the stress concentration during deformation. As shown in Fig. 2b, the nano-particle strings and the plate-like particles were not observed in sample E100. Instead, a large number of nano-particles (white arrows) are uniformly dispersed in the matrix. In addition, the LPSO phase is distributed along the extrusion direction (ED) (Fig. 2b) after hot extrusion. The SAED patterns recorded from LPSO phase

indicate that **this phase** has a 14H-type structure, Fig. 2c.

SEM-EDS and X-ray diffraction were conducted in order to further investigate the particle evolution during the thermo-mechanical processing. In **the** cast-T4 sample, the eutectic phase, as indicated with A, has a composition of Mg84.67RE11.42Zn3.91 (at.%). The LPSO phase, **as indicated with B**, has a composition of Mg87.63RE8.42Zn3.95 (at.%). After pre-ageing treatment at 410 °C for 1 h, the eutectic phase **particle C** and LPSO phase **particle D** show no significant change in **their** compositions. The composition of plate-like **particle E** is Mg95.50RE4.2Zn0.30 (at.%). As shown in Fig. 3c and d, the eutectic phase is observed **between** the LPSO phase in samples E10 and E100, and, the eutectic **phase** particles F and K have compositions **similar to that of** particles A and C. The LPSO phase particles G and L also have compositions **similar to that of** particles B and D. Thus, the pre-ageing and hot extrusion may **not** have **an** influence on the composition of eutectic phase and LPSO phase. The XRD results show Mg<sub>3</sub>RE phase and Mg<sub>12</sub>REZn phase co-exist in sample cast-T4, pre-aged sample A and E100 (Fig. 4). **Based on the SEM-EDS results and previous studies, the LPSO particles B, D, G and L can be identified as Mg<sub>12</sub>REZn phase [25]. The eutectic particles A, C, F and K thus should be Mg<sub>3</sub>RE phase or Mg<sub>3</sub>(RE, Zn) phase [26]. The observed stoichiometric ratio of Mg<sub>3</sub>(RE, Zn) phase is Mg:(RE+Zn) of 6:1, instead of the expected Mg:(RE+Zn) of 3:1. A possible explanation for this difference is the disturbance from α-Mg matrix on the SEM-EDS results. After pre-ageing (pre-aged sample A), Mg<sub>5</sub>RE phase was identified in the XRD patterns, thus, the plate-like particles are Mg<sub>5</sub>RE phase.**

In sample E10, the cracked plate-like particles are indicated as H and J and have compositions of Mg94.93RE4.71Zn0.36 (at.%) and Mg95.67RE4.00Zn0.33 (at.%),



respectively. The compositions of these particles are similar to that of particle E. The nano-particles form by breaking the plate-like particles. The SEM-EDS indicates that nano-particle I has a composition of Mg<sub>95.02</sub>RE<sub>4.56</sub>Zn<sub>0.42</sub> (at.%) which is close to that of particle H. The nano-particle I is expected to form from a plate-like particle similar to particle H. In sample E100, the nano-particle M also has similar composition to particles I and H. The Mg<sub>3</sub>RE, Mg<sub>5</sub>RE and Mg<sub>12</sub>REZn phases were identified in the XRD profile of sample E100 (Fig. 4), and based on this, these nano-particles are Mg<sub>5</sub>RE phase.

Fig. 5 shows the TEM images of pre-aged sample A and sample E10. As shown in Fig. 5a, the plate-like precipitates form in the matrix after pre-ageing and distribute in a triangle array with an angle of 60° between the three orientations. The selected area electron diffraction (SAED) pattern from the plate-like particle (white arrow) can be indexed according to the Mg<sub>5</sub>RE phase ( $\bar{F}4\bar{3}m$ ,  $a = 2.2$  nm) [11, 12]. The orientation relationship between Mg<sub>5</sub>RE phase and the  $\alpha$ -Mg matrix is such that  $(\bar{1}12)_{\text{Mg}_5\text{RE}} // (\bar{1}100)_{\alpha\text{-Mg}}$ ,  $[110]_{\text{Mg}_5\text{RE}} // [0001]_{\alpha\text{-Mg}}$ . A typical nano-particle string is shown in Fig. 5b, and a SAED pattern was obtained from the nano-particle indicated by a black arrow. This nano-particle has the same crystal structure as the plate-like particles, and can be indexed as the Mg<sub>5</sub>RE phase ( $\bar{F}4\bar{3}m$ ,  $a = 2.2$  nm) [11, 12]. The plate-like particles break into nano-particles but these nano-particles remain attached to each other (Fig. 5b). There is no phase transformations associated with breaking of plate-like particles. However, the volume fraction of Mg<sub>5</sub>RE phase decreased during the thermo-mechanical treatment, Table 2, from  $10.7 \pm 1.3\%$  in pre-aged sample A to  $6.6 \pm 0.4\%$  in sample E100. This decrease is due to the dissolution of Mg<sub>5</sub>RE phase during hot extrusion. The thermo-mechanical treatments (pre-aging and

extrusion) have negligible effect on the volume fraction of LPSO phase and Mg<sub>5</sub>RE phase.

### 3.2 Recovery and recrystallization

The nano-scale Mg<sub>5</sub>RE particles are on average less than 500 nm in size and are generally located at the grain boundaries and sub-grain boundaries (sub-GBs), Fig. 5c-e. In the regions close to the nano-scale Mg<sub>5</sub>RE particles, the dislocations nucleate and rearrange to form sub-GBs (Fig. 5c). When sub-GBs are free of particles they can move more easily, resulting in an increase in sub-grain size, until the sub-GBs nodes are pinned by Mg<sub>5</sub>RE particles (Fig. 5d and e). Thus, the nano-scale Mg<sub>5</sub>RE particles not only promote the formation of sub-GBs, but also prevent the sub-GBs migration through pinning.

Fig. 6a and b show a SEM image and corresponding EBSD inverse pole figure (IPF) map of sample E10. A comparison between Fig. 6a and b suggests that the small black spots and large black regions are nano-scale Mg<sub>5</sub>RE and LPSO precipitates, respectively. The high angle grain boundaries (> 15°, HAGBs) and the low angle grain boundaries (< 15°, LAGBs) were outlined by black and white lines, respectively. The micrograph shows a large number of equiaxed grains, indicating that DRX occurs during hot extrusion. Some coarse un-DRXed grains still remained in the alloy as highlighted by the black squares in Fig. 6a and b. The highlighted coarse un-DRXed grains region (Fig. 6a and b) was enlarged for further investigation (Fig. 6c and d). The subdivisions were observed within these un-DRXed grains, namely, sub-GBs which are indicated by black arrows. Nano-scale Mg<sub>5</sub>RE particles (black arrowheads 1-6) are associated with both LAGBs and HAGBs, are indicated by black arrowheads 1'-6' in Fig. 6d.

Small grains (white arrows in Fig. 6c) nucleate within a cluster of Mg<sub>5</sub>RE particles, and

these grains do not grow further due to the pinning caused by the nano-particle clusters [18]. It is noteworthy that the un-DRXed grains were sub-divided into small sub-grains, which are similar in size to the nearby DRXed grains in Fig. 6b and c. The DRXed grains transform from the sub-grains as the particles impede the migration of both grain and sub-grain boundaries through pinning. Thus, the nano-scale Mg<sub>3</sub>RE particles cause the subdivision of parent grains, and refine the newly recrystallized grains. A histogram showing the misorientation angle distributions for the samples E10 and E100 are shown in Fig. 6e. The number fraction of grain boundaries with low misorientation angle (< 15°) decreases from ~0.3 in the sample E10 to ~0.1 in the sample E100. In contrast, the fraction of grain boundaries with high misorientation angles (> 45°) in the sample E100 is higher than that in the sample E10, indicating that DRXed grains evolve from transformation of LAGBs to HAGBs. This alloy has a weak texture constituted by two texture components as shown in Fig. 6f. The maximum intensity of the texture is 1.30 multiples of a random distribution (MRD). The investigation of the texture evolution is beyond the scope of this publication and will be discussed in a future contribution.

### 3.3 Mechanical behaviours

Both the tensile and the compressive mechanical properties of the as-extruded samples are summarized in Table 2. The alloy exhibits an ultimate tensile strength ( $\sigma_{UTS}$ ) of  $362.5 \pm 3.2$  MPa, a 0.2 % proof stress ( $\sigma_{TPS}$ ) of  $305.7 \pm 1.0$  MPa and an elongation to failure ( $\epsilon_{TF}$ ) of  $6.2 \pm 0.9$  %. The compressive properties show an ultimate compressive strength ( $\sigma_{UCS}$ ) of  $540.2 \pm 4.4$  MPa, a 0.2 % proof stress ( $\sigma_{CPS}$ ) of  $362.7 \pm 1.4$  MPa and an elongation to failure ( $\epsilon_{CF}$ ) of  $10.5 \pm 0.2$  %. The calculated compression/tension yield asymmetry ( $\sigma_{CPS}/\sigma_{TPS}$ ) is

greater than unity, at 1.2.

The bright field (BF) TEM image of an extruded sample deformed to a total tensile strain of 3.3 % shows the stacking faults (SFs) **inside** the grain, Fig. 7a. In addition, a large number of dislocations were observed in the region between the SFs traversing **through** the matrix as indicated by **the** black arrows. As the majority of dislocations slip parallel to the basal plane, the basal slip tends to dominate in tension. In contrast, the BF TEM image of the as-extruded sample deformed to a total compressive strain of 2.9 % contains only few dislocations on the basal plane (black arrow), instead, many dislocations slip on the non-basal plane as indicated by white arrows, Fig. 7b. The non-basal dislocation slip is activated in compression, and the non-basal dislocations are pinned by the SFs. In addition, the dislocation arrays are evident, as indicated by white arrowheads, **Fig. 7c**. These arrays consisted of parallel dislocations and they sub-divide the grain in to small cells. The characteristics of **these** sub-grain boundaries indicate that recovery takes place during compression at ambient temperature.

The microstructure near the fracture surface of the as-extruded sample is shown in Fig. 8a-c. As indicated by white arrows in Fig. 8a, the cracks initiated in LPSO phase particles, and **traverse through the LPSO phase**, while they rarely propagated into the Mg matrix. Generally, the cracks stopped at the interface between LPSO phase and  $\alpha$ -Mg matrix, and the cracks are not observed in the region between LPSO phase particles. Thus, the LPSO phase serves as a crack source during tensile deformation. With the increase in **the** tensile load, the Mg/LPSO interface cannot prevent the propagation of cracks **which** resulted in fracture. The cracks propagated along the grain boundaries as indicated by white arrowheads in the Fig. 8b. The alloy failed by intergranular fracture in tension. Several shear bands initiated in the LPSO

phase as indicated by white arrowheads, Fig. 8c, (BF TEM image) and propagated across the LPSO phase in a same direction as the cracks, and terminated at the Mg/LPSO interface. The shear bands provide nucleation sites for microvoids, leading to fracture along the shear bands in the LPSO phase during tensile deformation.

In **compression**, the fracture did not occur in LPSO phase particles or at the Mg/LPSO interface, instead, it initiated in the matrix between LPSO phase particles as shown in Fig. 8d. The crack propagated in a direction approximately  $42^\circ$  from the ED through the grain as indicated by black arrowheads in Fig. 8d. **The alloy failed in transgranular manner**. It is noteworthy that the crack ended at **the** LPSO particle as indicated by black arrow. **The** LPSO phase serves as an obstacle for the crack propagation in compression. Moreover, the LPSO phase itself deformed **by** kinking as indicated by white arrows in Fig. 8d and e.

## 4. Discussion

### 4.1 Particles and recrystallization

The breaking and spheroidizing process of plate-like  $Mg_5RE$  particles and the dynamic recrystallization of grains are illustrated with the schematic diagrams in Fig. 9a-e. Pre-ageing increased the amount of plate-like  $Mg_5RE$  precipitates. **These** precipitates have a good thermal stability so that they cannot fully be dissolved into matrix by simply increasing the temperature or duration of ageing treatment (Fig. 1). At the initial stage of hot extrusion, the plate-like  $Mg_5RE$  particles do not fully dissolve into the matrix (Fig. 2a), instead, particles crack. No further phase transformation occurs during formation of cracks as  $Mg_5RE$  phase is an equilibrium phase [11, 12]. Severe deformation leads to a high dislocation density in the

vicinity of Mg<sub>5</sub>RE particles [20, 27-29], and the introduction of the dislocations enhances the diffusion of REs in the matrix so that the Mg<sub>5</sub>RE particles become thermally unstable. As a result, Mg<sub>5</sub>RE fragments gradually dissolve in the matrix, especially at sharp angular edges. The irregular fragments eventually evolve into isolated globular particles. With further deformation, the continued dissolution of Mg<sub>5</sub>RE fragments leads to a reduction of the volume fraction of Mg<sub>5</sub>RE phase (Table 2). The Mg<sub>5</sub>RE particle strings consequently disappear, instead, the globular Mg<sub>5</sub>RE particles become uniformly dispersed (Fig. 2b). In addition to **formation of cracks** and spheroidization, the dynamic precipitation introduces the globular Mg<sub>5</sub>RE particles during hot extrusion. However, the large decrease of the volume fraction of Mg<sub>5</sub>RE phase in sample E100 indicates that the dynamic precipitation contributes little to the formation of globular Mg<sub>5</sub>RE particles.

The dynamic recrystallization occurs in conjunction with the breaking of plate-like Mg<sub>5</sub>RE precipitates (Fig. 9c-e). In the alloys containing few particles, Robson et al [18] suggested that the dynamic recrystallization mainly occurs **in** regions near **the** grain boundaries where a large lattice **distortions are already** present. The abundant globular Mg<sub>5</sub>RE precipitates form in this alloy during pre-ageing and hot-extrusion. In the regions containing Mg<sub>5</sub>RE precipitates, geometrically necessary dislocations (GNDs) could nucleate and rearrange to form sub-GBs due to the lattice rotation and the release of a large amount of stored strain energy [20, 27-29]. Consequently, the parent grains subdivide into small cells. When a sub-GBs node is free of particles it would move more easily, and reduction in dislocation density of the sub-GBs is evident. These lead to coarsening of the sub-grains and increase in the misorientation between adjacent sub-grains [20]. In contrast, when newly

formed sub-GBs are pinned by the Mg<sub>5</sub>RE precipitates, the globular Mg<sub>5</sub>RE precipitates continuously accumulate GNDs (Fig. 5c-e and Fig. 6c). The blocked sub-grains transform into recrystallized grains without measurable changes in dimensions by increasing the sub-GBs misorientations until all the LAGBs are transformed into HAGBs (Fig. 6e). The recrystallized grains **form eventually** as a result of sub-GBs evolution which is activated by globular Mg<sub>5</sub>RE precipitates [20]. This dynamic recrystallization process is identified as continuous DRX [30].

## 4.2 Microstructures and strengthening

The microstructures obtained by the thermo-mechanical treatments described here contributed to the improved mechanical properties of the alloy investigated (Table 3). The strengthening of Mg alloys is strongly affected by grain refinement; basal fibre texture and second phase particles [4, 17, 19]. The average grain size of DRXed grains is 3.6 μm, which **led** to a high yield stress due to the Hall-Petch strengthening. **The grain boundaries pinned by the Mg<sub>5</sub>RE particles during hot extrusion resulted in the observed grain refinement. The large volume fraction of the globular Mg<sub>5</sub>RE particles and their dense distribution at grain boundaries strengthened** this alloy by preventing the rotation of grains and **pinning** the grain boundaries [3, 16, 17].

In tension, the fracture propagated along the grain boundaries, indicating that the interface between Mg<sub>5</sub>RE phase and grains was weak, **which** provided a preferential path for crack propagation. The alloy fractured in an intergranular manner. The Mg<sub>5</sub>RE phase did not serve as source for the initiation of cracks, **but** the cracks initiated at the LPSO phase particle, and propagated into the Mg matrix. The (0001)<sub>LPSO</sub> is parallel to the layered interface of

LPSO phase, and the  $(0001)\langle 11\bar{2}0 \rangle$  basal slip is the dominant deformation mode at room temperature [21, 23]. As the layered interface was aligned to the ED after hot extrusion, the tensile load was applied parallel to  $(0001)_{\text{LPSO}}$  in a hard orientation for the basal slip in the LPSO phase. Thus the deformation along basal plane was suppressed in the LPSO phase. However, with the increase in tensile load, the LPSO phase can be deformed by formation of shear bands (Fig. 8). Subsequently, microvoids nucleate preferentially at the shears bands due to local stress concentrations [27, 31]. The fracture propagates along the shear bands in the LPSO phase perpendicular to ED, and the LPSO phase not only serves as reinforcement, but also acts as a source of cracks in tension.

In compression, the kink bands were observed inside the LPSO particles, which are beneficial for the compressive deformation as kinks could accommodate the strain concentration near the LPSO phase and at the Mg/LPSO interface [23]. It has been proposed that the kinking leads to work hardening of the LPSO particles [24]. Thus, the LPSO phase contributed to strengthening of this alloy in compression, and no microscopic cracks were observed in the LPSO particles or at the Mg/LPSO interfaces after compression (Fig. 8b). In contrast, the cracks preferentially occur in the region between the adjacent LPSO phase particles and propagates through the grains. The crack terminated at the LPSO particles, and in compression the alloy failed in a transgranular manner. Shao et al. [24] suggested that the LPSO/LPSO interfaces and Mg/LPSO interfaces were not favoured nucleation sites for crack formation during compression. As a hard phase, the LPSO particles efficiently prevent catastrophic failure by hindering the propagation of cracks. The large volume fraction of aligned LPSO phase not only strengthens the alloy through the short-fiber strengthening [21],



but also **contributes differently** in the failure of the alloy in tension and compression.

### 4.3 Yield strength asymmetry

In Mg extrusions, the yield asymmetry, i.e. the ratio between  $\sigma_{\text{CPS}}/\sigma_{\text{TPS}}$ , is related to the texture, deformation mode and grains size [32, 33]. Generally, it is between 0.3 and 0.7 [33]. The strong basal fibre texture favours twinning in compression and not in tensile loading along the ED, resulting in a large yield asymmetry. **A weak texture and fine grains are required to decrease the yield asymmetry, as the non-basal and basal slip become easily activated and twin activity reduced** [32, 34]. **In this alloy**, a  $\sigma_{\text{CPS}}/\sigma_{\text{TPS}}$  ratio is 1.2 with higher compressive yield strength than tensile yield strength.

Twinning was rarely observed in this alloy during deformation due to the grain refinement, weak texture and dense distribution of SFs [24, 33, 35], and has a negligible effect on the yield asymmetry. The basal slip was the dominant deformation mode in tension at room temperature (Fig. 7a). The dense SFs, which were parallel to basal plane of  $\alpha$ -Mg matrix, contributed little to hinder basal slip. In contrast, the non-basal slip was activated during **compressive deformation** (Fig. 7b). The SFs efficiently impeded the glide of non-basal dislocations, resulting in the strain concentration and dislocation entanglements in the matrix (Fig. 7b). The interaction between high density of SFs and the dislocations **resulted in work hardening**. Consequently, the compressive yield strength of the alloy increased. The assembly of dense dislocations promoted the formation of sub-GBs (Fig. 7c), which caused the parent grain to subdivide into small sub-grains. It has been established previously that the sub-grains strengthen the alloys by contributing to work hardening [36, 37]. The sub-GBs can produce effective obstacles to the dislocation propagation. Thus, the sub-grains contribute to the

enhanced yield strength in compression.

The **yield asymmetry** of this alloy is also attributed to the deformation asymmetry of LPSO phase. The LPSO phase serves as a crack source, and the brittle grain boundaries contribute to propagation of cracks leading to fracture in tension. In contrast, during compression the LPSO phase did not serve as a crack source, but became an obstacle to the propagation of cracks. As a result, the alloy has relatively low yield strength in tension, but higher yield strength in compression. **The yield asymmetry observed** is beneficial **for** the further design and application of Mg extrusions.

## 5. Conclusions

1. Pre-ageing significantly increased the volume fraction of plate-like Mg<sub>5</sub>RE phase. These plate-like particles transform to nano-scale globular particles by the breaking and spheroidization during hot extrusion.
2. The globular Mg<sub>5</sub>RE particles not only contribute to the continuous DRX by promoting the evolution of sub-GBs from low to high misorientation, but also lead to grain refinement through particle pinning.
3. The LPSO phase deforms via shear band and serves as a source of cracks in tension, but deforms through **kinking** and **acts** as a barrier for fracture in compression.
4. The grain refinement, nano-scale globular Mg<sub>5</sub>RE and LPSO phases contribute to tensile and compressive mechanical properties for the alloy. The yield strength asymmetry is attributed to the deformation asymmetry of LPSO phase and the different deformation behaviour of  $\alpha$ -Mg matrix in tension and compression.

## Acknowledgement

The authors thank Dr. Jan Bohlen and Dr. Francesco D'Elia for their fruitful discussion. Prof. F. Pyczak and Mr. U. Lorenz are acknowledged for the provision of access to the TEM facilities at Helmholtz Zentrum Geesthacht. This work is supported by the National Key Technologies R&D Program (2012BAE01B04, 2012DFH50100, KGFZD-125-13-021, 201001C0104669453). Zijian Yu would like to thank the Chinese Academy of Sciences and German Academic Exchange Service (CAS-DAAD) scholarship program for the financial support.

## References

- [1] C. Xu, M.Y. Zheng, S.W. Xu, K. Wu, E.D. Wang, S. Kamado, G.J. Wang, X.Y. Lv, *Materials Science and Engineering: A*, 547 (2012) 93-98.
- [2] K. Liu, X. Wang, W. Du, *Materials Science and Engineering: A*, 573 (2013) 127-131.
- [3] Z.J. Yu, Y. Huang, X. Qiu, Q. Yang, W. Sun, Z. Tian, D.P. Zhang, J. Meng, *Materials Science and Engineering: A*, 578 (2013) 346-353.
- [4] T. Homma, N. Kunito, S. Kamado, *Scripta Materialia*, 61 (2009) 644-647.
- [5] K.H. Yoshihito Kawamura, Akihisa Inoue and Tsuyoshi Masumoto, *Materials Transactions*, 42 (2001) 1172-1176.
- [6] H. Somekawa, A. Singh, T. Mukai, *Scripta Materialia*, 56 (2007) 1091-1094.
- [7] X. Hou, Z. Cao, L. Zhao, L. Wang, Y. Wu, L. Wang, *Materials & Design*, 34 (2012) 776-781.
- [8] Z. Leng, J. Zhang, T. Zhu, R. Wu, M. Zhang, S. Liu, J. Sun, L. Zhang, *Materials & Design*, 52 (2013) 713-719.
- [9] K. Yamada, H. Hoshikawa, S. Maki, T. Ozaki, Y. Kuroki, S. Kamado, Y. Kojima, *Scripta Materialia*, 61 (2009) 636-639.
- [10] X. Gao, S.M. He, X.Q. Zeng, L.M. Peng, W.J. Ding, J.F. Nie, *Materials Science and Engineering: A*, 431 (2006) 322-327.
- [11] J.F. Nie, B.C. Muddle, *Acta Materialia*, 48 (2000) 1691-1703.
- [12] J.F. Nie, B.C. Muddle, *Scripta Materialia*, 40 (1999) 1089-1094.
- [13] X. Gao, J.F. Nie, *Scripta Materialia*, 58 (2008) 619-622.
- [14] T. Honma, T. Ohkubo, S. Kamado, K. Hono, *Acta Materialia*, 55 (2007) 4137-4150.
- [15] J.F. Nie, *Scripta Materialia*, 48 (2003) 1009-1015.
- [16] S.W. Xu, N. Matsumoto, S. Kamado, T. Honma, Y. Kojima, *Materials Science and Engineering: A*, 517 (2009) 354-360.
- [17] S.W. Xu, K. Oh-ishi, S. Kamado, F. Uchida, T. Homma, K. Hono, *Scripta Materialia*, 65 (2011)

269-272.

- [18] J.D. Robson, D.T. Henry, B. Davis, *Acta Materialia*, 57 (2009) 2739-2747.
- [19] J. Bohlen, M.R. Nürnberg, J.W. Senn, D. Letzig, S.R. Agnew, *Acta Materialia*, 55 (2007) 2101-2112.
- [20] H. Ahlborn, E. Hornbogen, U. Köster, *Journal of Materials Science*, 4 (1969) 944-950.
- [21] K. Hagihara, A. Kinoshita, Y. Sugino, M. Yamasaki, Y. Kawamura, H.Y. Yasuda, Y. Umakoshi, *Acta Materialia*, 58 (2010) 6282-6293.
- [22] K. Hagihara, A. Kinoshita, Y. Fukusumi, M. Yamasaki, Y. Kawamura, *Materials Science and Engineering: A*, 560 (2013) 71-79.
- [23] K. Hagihara, N. Yokotani, Y. Umakoshi, *Intermetallics*, 18 (2010) 267-276.
- [24] X.H. Shao, Z.Q. Yang, X.L. Ma, *Acta Materialia*, 58 (2010) 4760-4771.
- [25] Y.M. Zhu, A.J. Morton, J.F. Nie, *Acta Materialia*, 60 (2012) 6562-6572.
- [26] S. Zhang, G.Y. Yuan, C. Lu, W.J. Ding, *Journal of Alloys and Compounds*, 509 (2011) 3515-3521.
- [27] M.F. Ashby, *Philosophical Magazine*, 21 (1970) 399-424.
- [28] F.J. Humphreys, *Acta Metallurgica*, 25 (1977) 1323-1344.
- [29] D. Kuhlmann-Wilsdorf, N. Hansen, *Scripta Metallurgica et Materialia*, 25 (1991) 1557-1562.
- [30] T. Sakai, A. Belyakov, R. Kaibyshev, H. Miura, J.J. Jonas, *Progress in Materials Science*, 60 (2014) 130-207.
- [31] S.E. Ion, F.J. Humphreys, S.H. White, *Acta Metallurgica*, 30 (1982) 1909-1919.
- [32] J. Bohlen, S. Yi, D. Letzig, K.U. Kainer, *Materials Science and Engineering: A*, 527 (2010) 7092-7098.
- [33] J. Bohlen, P. Dobroň, J. Swiostek, D. Letzig, F. Chmelík, P. Lukáč, K.U. Kainer, *Materials Science and Engineering: A*, 462 (2007) 302-306.
- [34] M.R. Barnett, A.G. Beer, D. Atwell, A. Oudin, *Scripta Materialia*, 51 (2004) 19-24.
- [35] M.R. Barnett, Z. Keshavarz, A.G. Beer, D. Atwell, *Acta Materialia*, 52 (2004) 5093-5103.
- [36] R. Sandström, *Acta Metallurgica*, 25 (1977) 905-911.
- [37] R. Sedláček, W. Blum, J. Kratochvíl, S. Forest, *Metallurgical and Materials Transactions A*, 33 (2002) 319-327.

Designation	History
Cast-T4	<ol style="list-style-type: none"> <li>1. As-cast sample</li> <li>2. <math>535 \pm 3</math> °C for 24 hours</li> </ol>
Pre-aged sample A	<ol style="list-style-type: none"> <li>1. Cast-T4</li> <li>2. <math>410 \pm 3</math> °C for 1 hour</li> </ol>
Pre-aged sample B	<ol style="list-style-type: none"> <li>1. Pre-aged sample A</li> <li>2. <math>430 \pm 3</math> °C for 2 hours</li> </ol>
Pre-aged sample C	<ol style="list-style-type: none"> <li>1. Pre-aged sample A</li> <li>2. <math>470 \pm 3</math> °C for 2 hours</li> </ol>
E10/E100	<ol style="list-style-type: none"> <li>1. Pre-aged sample A</li> <li>2. Hot extrusion (<math>410^{\circ}\text{C}</math>, 30:1, <math>1.0 \text{ mm}\cdot\text{s}^{-1}</math>)</li> <li>3. 10 mm/100 mm away from the front end of extruded bar</li> </ol>

Table 1. Designation and history of the studied samples.

Sample	Volume fraction (%)		
	Mg <sub>5</sub> RE phase	LPSO phase	Mg <sub>3</sub> RE phase
Cast-T4	0	8.2±0.6	1.6±0.4
Pre-aged A	10.7±1.3	8.3±1.5	1.3±0.5
Pre-aged B	10.2±0.7	9.0±0.6	1.3±0.5
Pre-aged C	4.9±1.5	8.5±1.8	1.5±0.6
E10	10.1±1.5	8.9±1.6	2.0±0.5
E100	6.6±0.4	7.3±1.3	1.0±0.3

Table 2. The volume fraction of Mg<sub>5</sub>RE phase particles in each sample. Note: Mg<sub>5</sub>RE phase exist in terms of plate like particle in pre-aged samples and in terms of irregular particles in samples E10 and E100.

Sample state	Measurement type	$\sigma_{TPS}$ and $\sigma_{CPS}$ (MPa)	$\sigma_{UTS}$ and $\sigma_{UCS}$ (MPa)	$\epsilon_{TF}$ and $\epsilon_{CF}$ (%)	Yield asymmetry ( $\sigma_{CPS}/\sigma_{TPS}$ )
As-extruded	Tensile test	$305.7 \pm 1.0$	$362.5 \pm 3.2$	$6.2 \pm 0.9$	1.2
	Compressive test	$362.7 \pm 1.4$	$540.2 \pm 4.4$	$10.5 \pm 0.2$	

Table 3 Tensile and compressive mechanical properties of as-extruded samples at room temperature (25 °C).

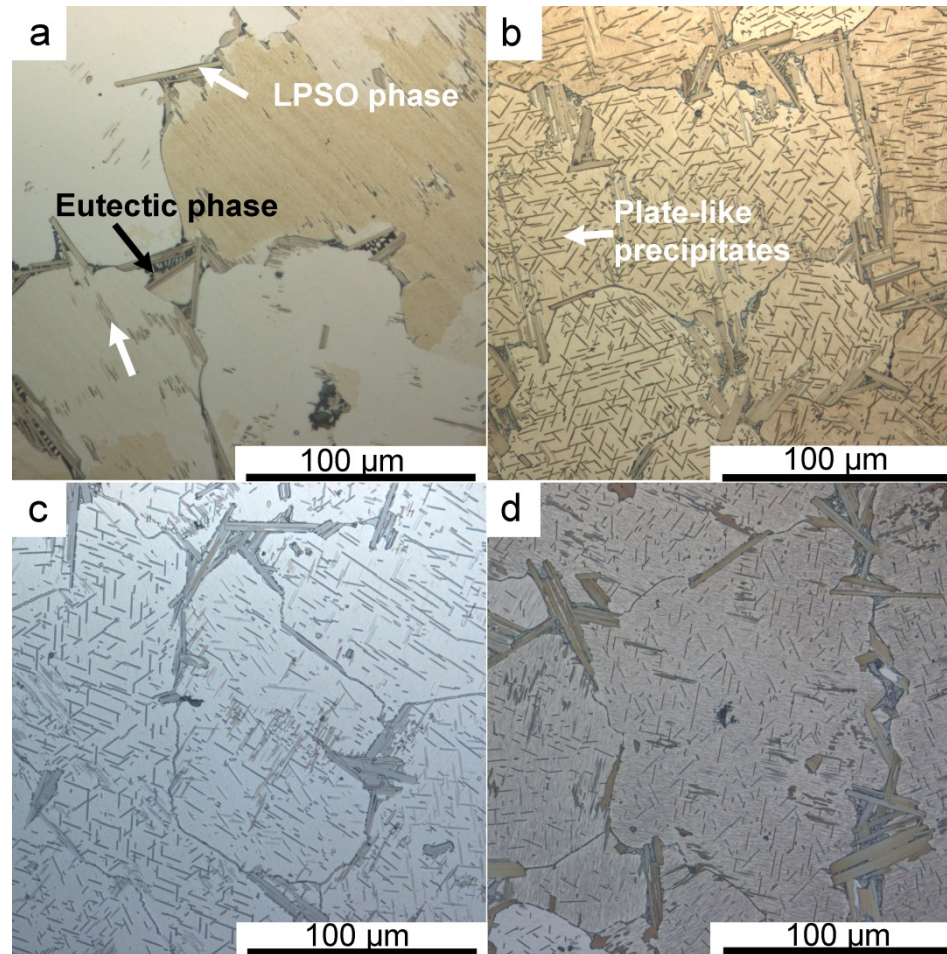


Fig. 1. OM images of (a) cast-T4 sample; (b) pre-aged A sample; (c) pre-aged B sample; (d) pre-aged C sample.



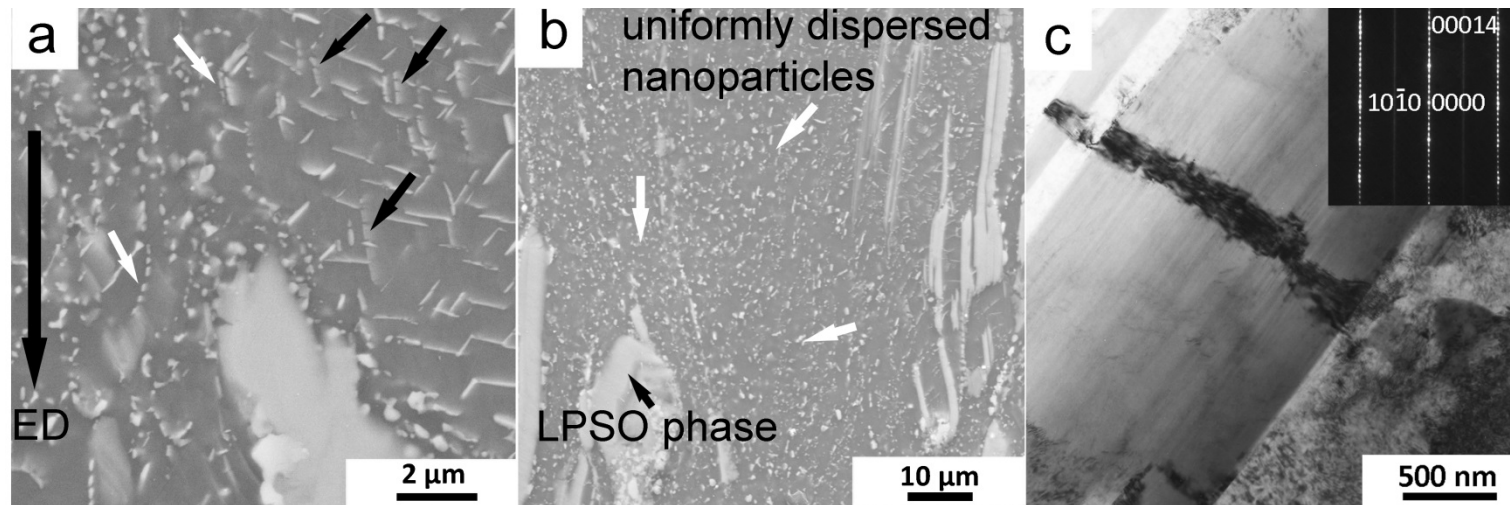


Fig. 2. SEM images of (a) E10 sample and (b) E100 sample. (c) TEM image of 14H-LPSO phase in E100 sample.

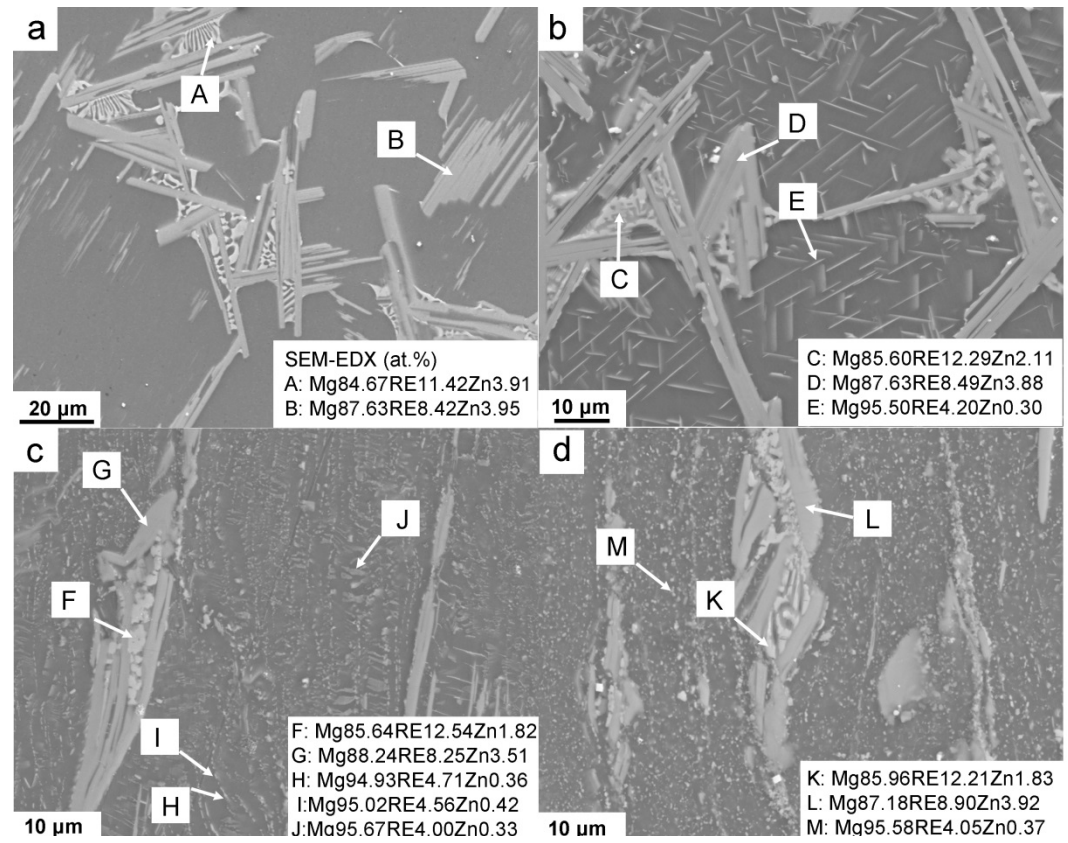


Fig. 3. SEM image of (a) cast-T4 sample; (b) pre-aged A sample; (c) E10 sample and (d) E100 sample. The EDS result to respective particle in each sample is shown in the insets. The particles are labeled by capital letters A to M.

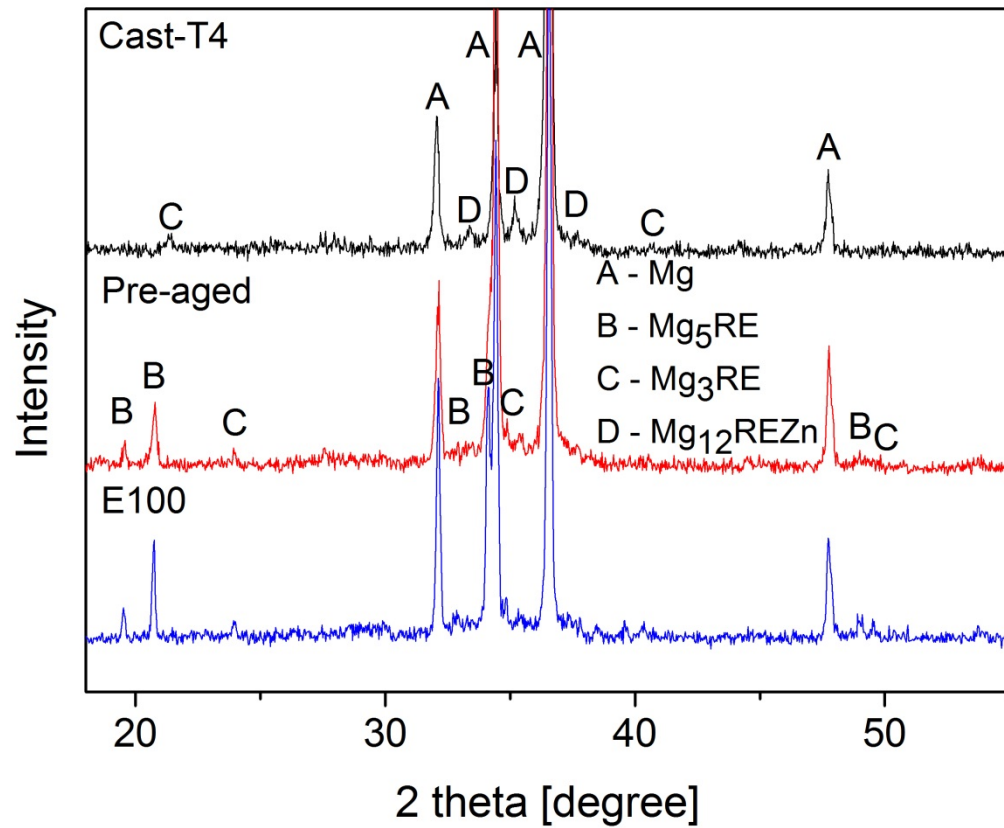


Fig. 4. X-ray diffraction patterns of cast-T4 sample, pre-aged A sample and E100 sample.

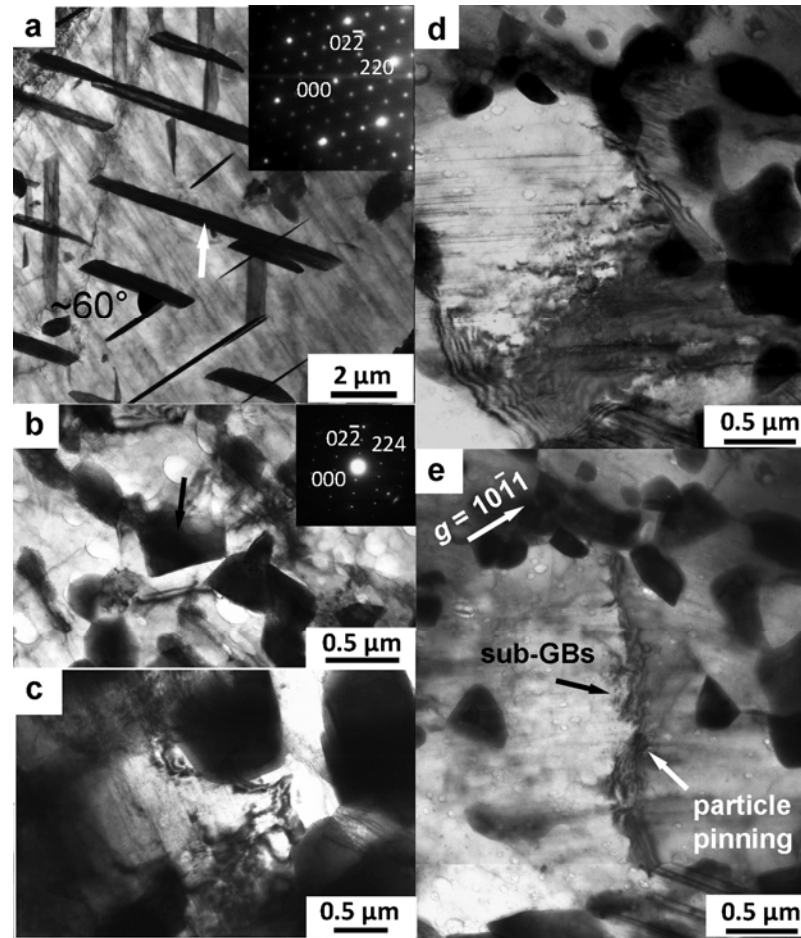


Fig. 5. TEM images and corresponding SAED patterns of (a) plate-like Mg<sub>5</sub>RE particle in pre-aged A sample; (b) Mg<sub>5</sub>RE particle string; (c) subgrains near globular Mg<sub>5</sub>RE particles and (d and e) sub-GBs in a subdivided grain in E10 sample.

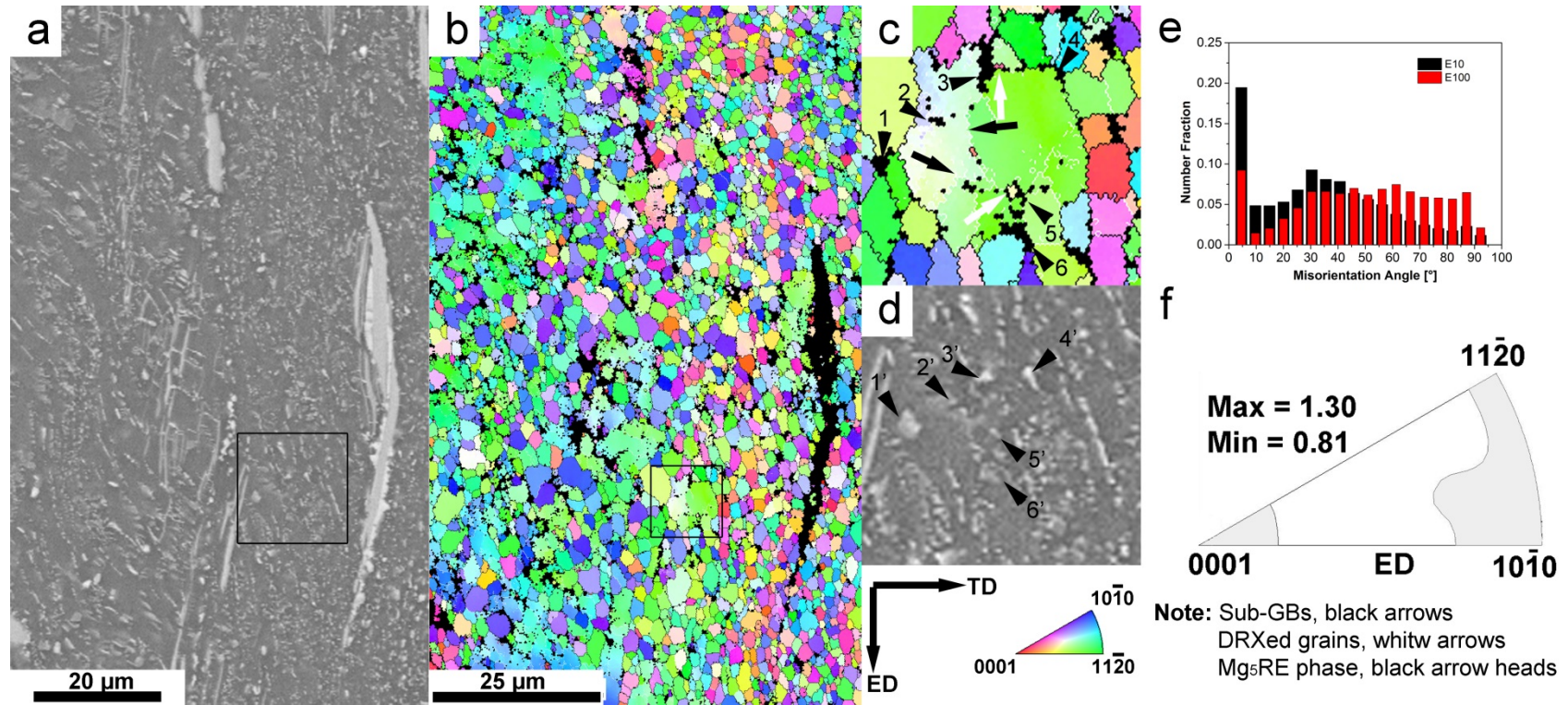


Fig. 6. (a) SEM image of E10 sample; (b) corresponding EBSD IPF map of image (a); (c) un-DRXed grains highlighted by the black square in image (a) and (b); (d) corresponding SEM image of the highlighted un-DRXed grains; (e) Misorientation Angle of E10 and E100 samples; (d) IPF of E100 sample.

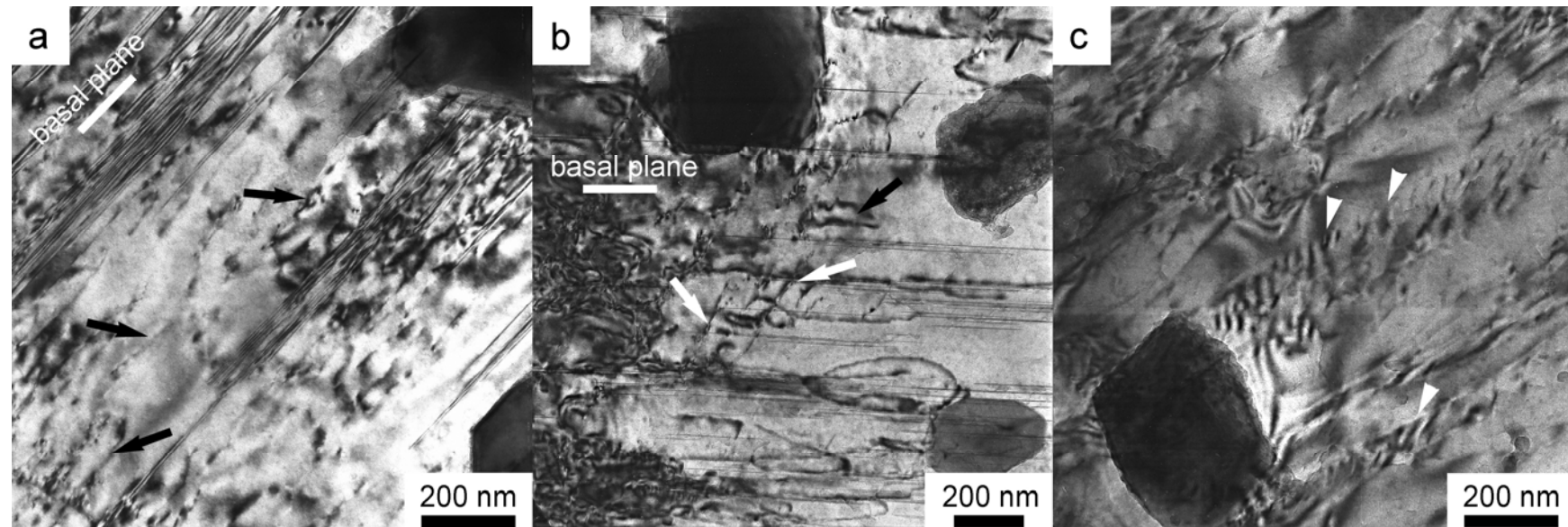


Fig. 7. TEM images of as-extruded sample (a) in tension with a strain of 3.33%; (b and c) in compression with a strain of 2.85%.

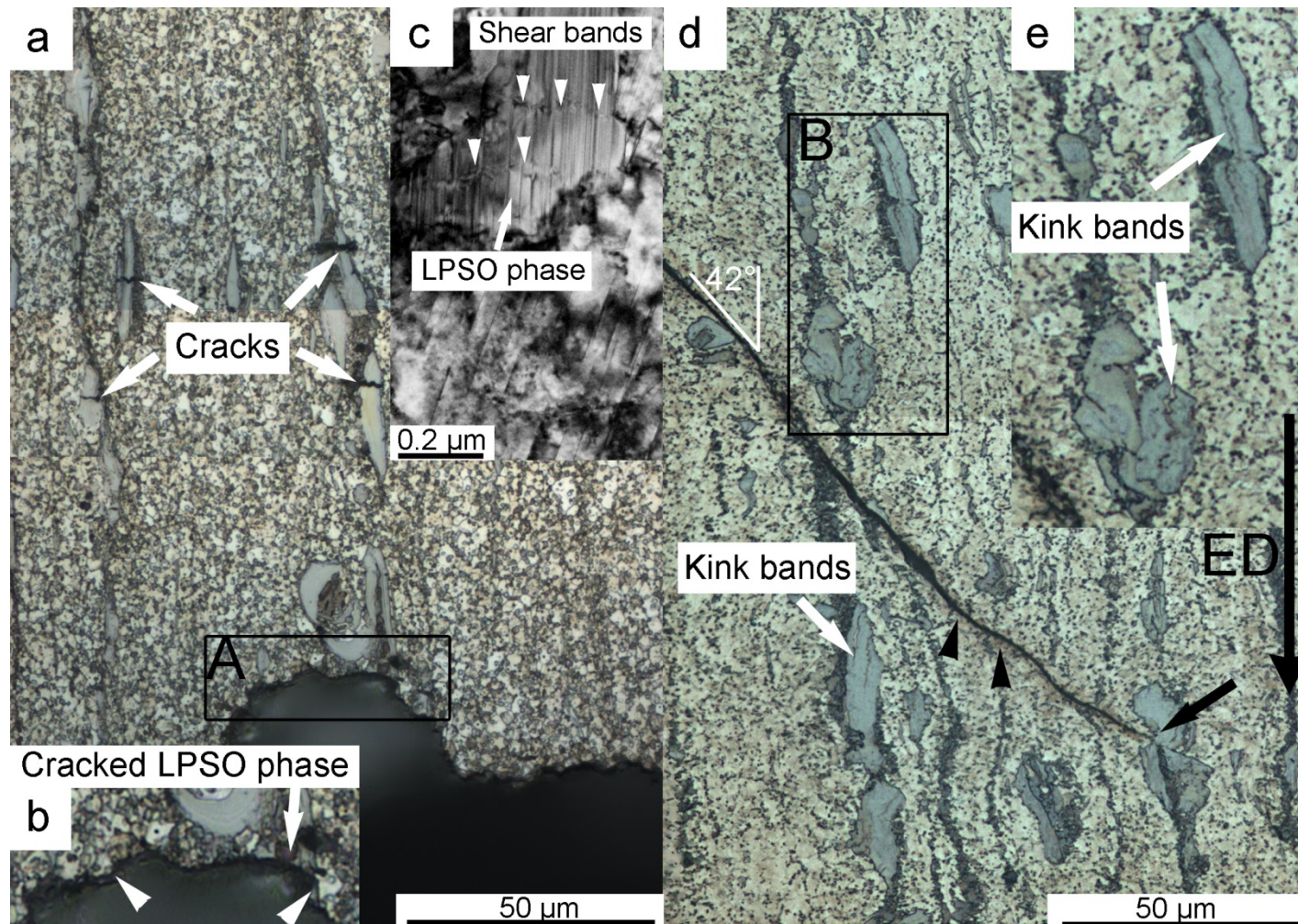


Fig. 8. Microstructure of as-extruded sample (a - c) after tensile test and (d and e) after compressive test. Image (b) is the enlargement of highlighted area A; and image (e) is the enlargement of highlighted area B.

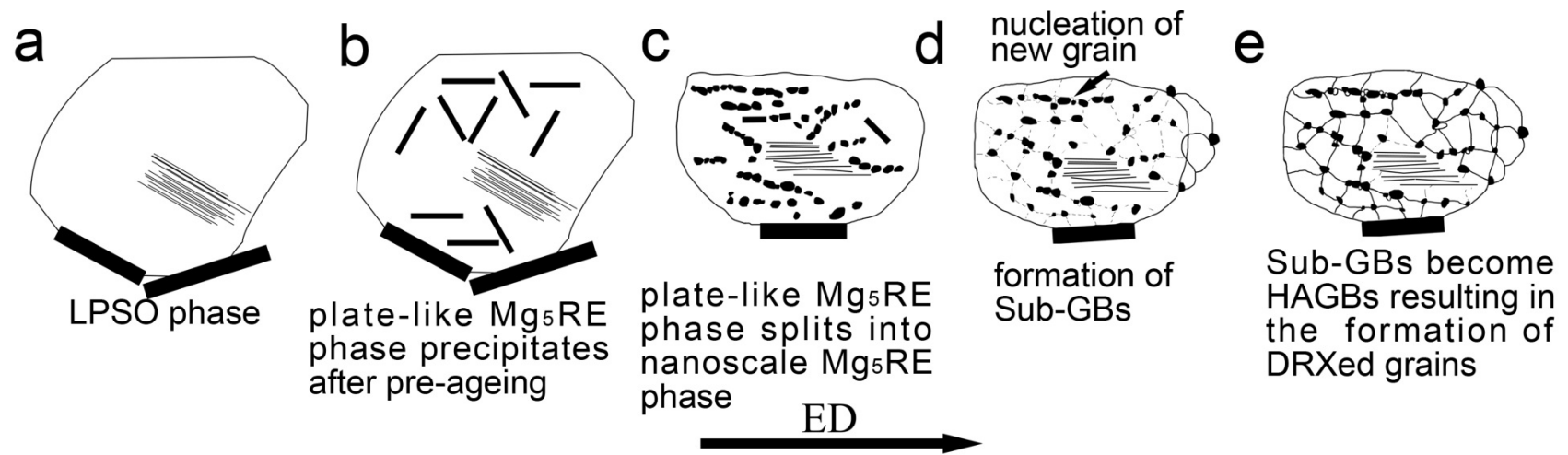


Fig. 9. Schematic illustration of microstructural evolution during thermomechanical treatments. (a) cast-T4 treatment; (b) pre-aged A treatment; (c-e) hot extrusion.